

---

# An Intrinsic Laser-Damage Mechanism in Next-Generation OMEGA UV Multilayer Coatings

Laser-induced damage has always been and remains as vexing as it is expensive. Despite a quarter century of work, the problem has not been eliminated or even fully defined—only the technical limits have been increased. Although dielectric thin films have improved over the last 25 years, they remain especially difficult subjects to deal with owing to the multiparameter nature of the nonequilibrium deposition methods used in their preparation. As new analytical methods and tools become available, however, better insight into the laser-damage enigma is gained.

The importance of nodular film-growth defects in originating laser damage was one such key insight that was recently offered through a series of pioneering papers by the Optical Coatings Group at Lawrence Livermore National Laboratory.<sup>1–4</sup> These results were achieved through a combination of (1) analytical modeling of laser-field effects in and around growth nodules; (2) mapping of these growth nodules under atomic-force microscopy; and (3) physical analysis of the nodules by focused-ion-beam cross sectioning and Auger spectroscopy. In conjunction with conventional laser-damage-threshold measurements, this approach yielded the broad conclusion that nodular growth defects are the dominant laser-damage drivers in thin films. From a systems design viewpoint, nodules became the coating affliction to be eradicated for laser-damage thresholds to improve.

As results for the fundamental and second-harmonic-wavelength laser-damage characteristics of multilayer coatings were being disseminated, prototype development and actual production of OMEGA Upgrade transport coatings were proceeding at LLE. In this article we report our observations on laser damage in these  $3\omega$  (351-nm) high reflectors (HR's), obtained by combining conventional  $3\omega$  laser-damage investigations with mapping of damaged and undamaged sites on production witness pieces by atomic force microscopy. These findings differ from the earlier ones for 1054-nm and 527-nm conditions in that the nodules are capable of surviving fluences that cause crater formation by other mechanisms. These mecha-

nisms confine crater origination to the top two layers of the multilayer, high-reflector stack.

## Samples and Experimental Conditions

Two types of oblique-incidence,  $3\omega$  high reflectors were analyzed: (1) a  $46^\circ$  angle-of-incidence, 37 alternating quarter-wave stack HR made from  $\text{HfO}_2$  and  $\text{SiO}_2$ , with the first and third  $\text{HfO}_2$  layers replaced by  $\text{Sc}_2\text{O}_3$  to make the coating strippable; and (2) a  $50^\circ$  angle-of-incidence, 53 alternating quarter-wave stack of  $\text{Sc}_2\text{O}_3$  and  $\text{SiO}_2$ , with 47 layers of exact quarter-wave optical thicknesses and the top six layers adjusted in thickness for reduced electric-field intensity at the layer interfaces. Both coatings were deposited by conventional e-beam methods. One of the primary goals in the deposition process was to minimize the formation of growth nodules.

Witness pieces from these production coatings were irradiated at the respective angles using frequency-tripled, 0.7-ns pulses from a Nd:glass slab laser. At optimized conversion efficiency and under weak focusing by a 10-m focal-length silica lens, fluences up to  $14 \text{ J/cm}^2$  within a  $600\text{-}\mu\text{m}$  spot diameter were delivered to the test piece. Damage was identified by dark-field microscopy (110-times magnification) as agglomeration of very fine, low-light-level scattering sites (nebula). The damage thresholds in 1-on-1 irradiation mode ( $p$ -polarization, scaled to  $0^\circ$  incidence for systems design engineering convenience) were  $5.6 \pm 0.2 \text{ J/cm}^2$  in the case of the  $\text{HfO}_2/\text{SiO}_2$  system, and  $5.4 \pm 0.1 \text{ J/cm}^2$  for  $\text{Sc}_2\text{O}_3/\text{SiO}_2$ . Sites later mapped by atomic force microscopy experienced damage at  $\sim 5\%$  above threshold (defined as “weak” damage sites) and at  $15\%$ – $20\%$  above threshold fluences (defined as “moderate” damage sites).

Analysis of both irradiated and unirradiated (control) sites was carried out using a Nanoscope III (Digital Instruments, Inc.) atomic force microscope (AFM) operated in contact mode. “Oxide-sharp”  $\text{Si}_3\text{N}_4$  probes proved adequate for resolving both nanometer-scale film morphology and any laser-modified structures, although rapid wear required fre-

quent probe replacement. Typical “stickiness” between the sample and probe of dielectric oxide films during scans was counteracted by making adjustments in scanning speeds and feedback loop parameters. The contact force was routinely minimized to ensure an unmodified scan area during repeated scans. Adjacent,  $5\text{-}\mu\text{m} \times 5\text{-}\mu\text{m}$  sections were mapped with the goal of accumulating statistically significant numbers of various damage features, such as cracks, craters, or domes. For a given sample and irradiation condition, this number is of the order of 100 for each irradiated site. Each feature observed was subsequently analyzed in high-resolution closeups.

**Results and Discussion**

**1. Morphology of Unirradiated Films**

In both the  $\text{HfO}_2/\text{SiO}_2$  and  $\text{Sc}_2\text{O}_3/\text{SiO}_2$  stacks, the terminating (top) layer is the respective high-refractive-index medium (i.e.,  $\text{HfO}_2$  or  $\text{Sc}_2\text{O}_3$ ). Figures 62.1 and 62.2 show the typical oxide-film columnar structures for these materials, with 25- to 40-nm grain size and 3.3- to 3.6-nm vertical rms roughness. Taking into account an AFM probe tip radius  $R_{\text{tip}} \sim 10$  nm (according to manufacturer specifications) and the recently reported image-distortion criterion,<sup>5</sup> i.e.,  $R_{\text{grain}}/R_{\text{tip}} < 2$ , we find our imaged grain size to be overestimated. The magnitude of this error, however, is not large, as we were able to resolve the 10-nm-scale granular structure of  $\text{Ta}_2\text{O}_5$  monolayer films using the same probes.<sup>6</sup> These features are less than half the scale length of the  $\text{HfO}_2$  and/or  $\text{Sc}_2\text{O}_3$  characteristic grains.

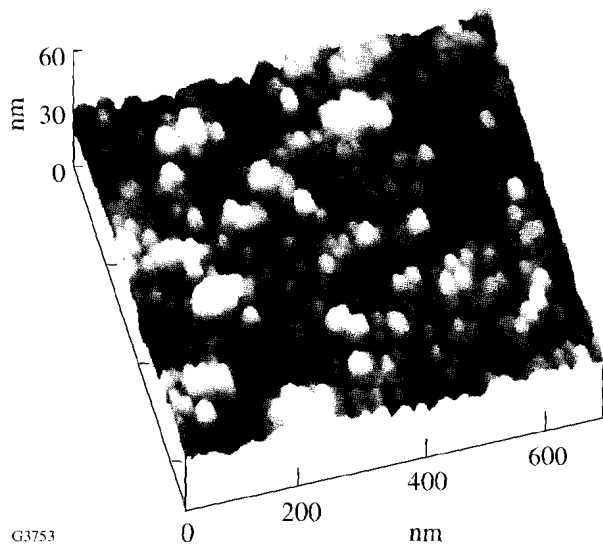


Figure 62.1  
Columnar structure of the  $\text{HfO}_2$  top surface ( $700 \times 700\text{-}\mu\text{m}$  scan) of a  $\text{HfO}_2/\text{SiO}_2$  multilayer HR stack.

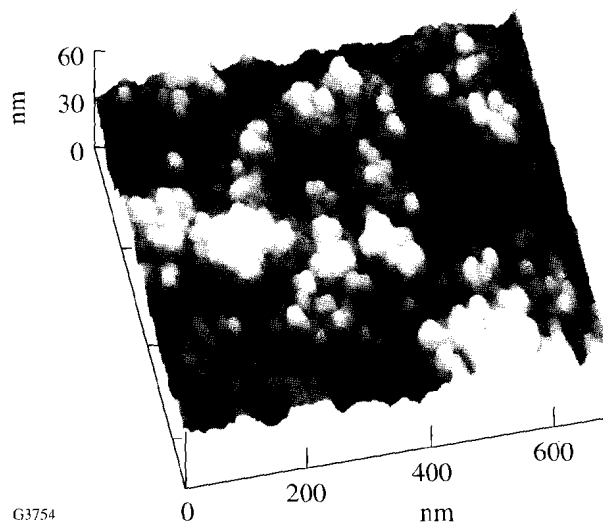


Figure 62.2  
Columnar structure of the  $\text{Sc}_2\text{O}_3$  top surface ( $700 \times 700\text{-}\mu\text{m}$  scan) of a  $\text{Sc}_2\text{O}_3/\text{SiO}_2$  multilayer HR stack with reduced  $E$ -field design.

**2. Laser-Induced Morphology**

In both  $\text{HfO}_2/\text{SiO}_2$  and  $\text{Sc}_2\text{O}_3/\text{SiO}_2$  coatings, craters on the scale of 200 nm to 700 nm across and up to 130 nm deep are the main laser-damage features (Figs. 62.3 and 62.4). Their spatial correlation with the incident beam-fluence profile recorded in a sample equivalent plane by a CID camera is weak or nearly nonexistent. Under weakly damaging conditions,

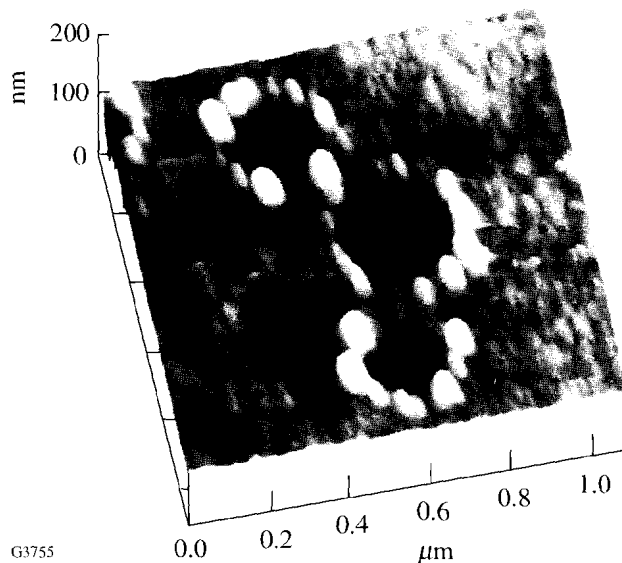


Figure 62.3  
Conventional laser-damage craters formed by 351-nm radiation in the  $\text{HfO}_2/\text{SiO}_2$  film. The area shown corresponds to the periphery of a moderate-damage site.

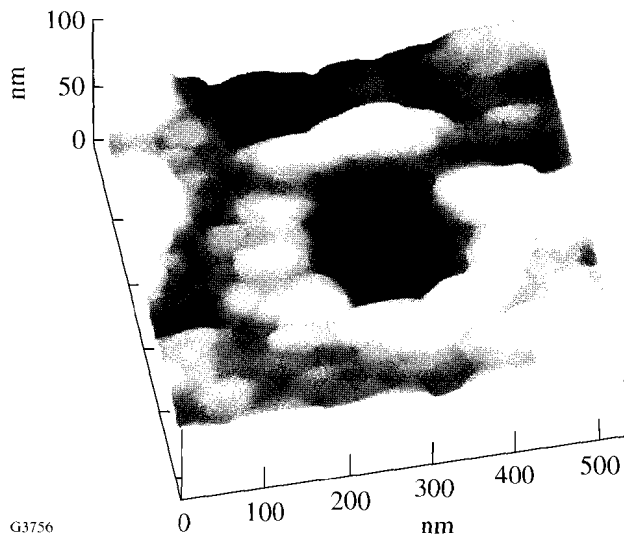


Figure 62.4  
Conventional laser-damage crater formed by 351-nm radiation in the  $\text{Sc}_2\text{O}_3/\text{SiO}_2$  film. The crater is 38 nm deep and, on average, 300 nm in diameter.

crater-to-crater average distances are  $2.4 \mu\text{m}$  for  $\text{HfO}_2/\text{SiO}_2$  and  $2.7 \mu\text{m}$  for  $\text{Sc}_2\text{O}_3/\text{SiO}_2$ . In agreement with our earlier findings on 1054-nm laser-irradiated monolayer films,<sup>6</sup> such craters develop independently of whether or not micron-scale growth nodules are present. Figure 62.5 demonstrates that growth nodules and inclusions can remain unaffected, even under 351-nm irradiation, while other defect-driving mecha-

nisms dominate crater formation in the nodules' immediate vicinity. Up to now, we have been unable to offer similar evidence for 1054-nm HR stacks. Within that constraint, the current evidence suggests that growth nodules *are not always* the dominating cause of damage. We have, in fact, no AFM evidence or visible-light microscopy record for any observable feature that could be used as a landmark for predicting the occurrence of these craters.

Closer analysis of these craters offers some interesting conclusions regarding their potential source. In agreement with LLNL findings from 1981,<sup>7</sup> under near-threshold conditions the majority of craters are very shallow, originating in either or both of the top two layers: i.e., 29% of  $\text{HfO}_2/\text{SiO}_2$  craters and 17% of  $\text{Sc}_2\text{O}_3/\text{SiO}_2$  craters are less than 20 nm deep. If a compact absorber is postulated as the damage originator, one can deduce immediately from this crater depth that such an absorber would have to be limited in extent to  $\sim 10$  nm.

Modern AFM tools now permit greater insight into crater cross-sectional features than were observed 14 years ago. We have found many instances in which a conventional, conedged crater is superimposed on a second, deeper crater (see Fig. 62.6). These complex craters occur mainly in  $\text{Sc}_2\text{O}_3/\text{SiO}_2$  with an abundance level of 37%. Conventional craters show conical walls that are normally smooth and without any grain

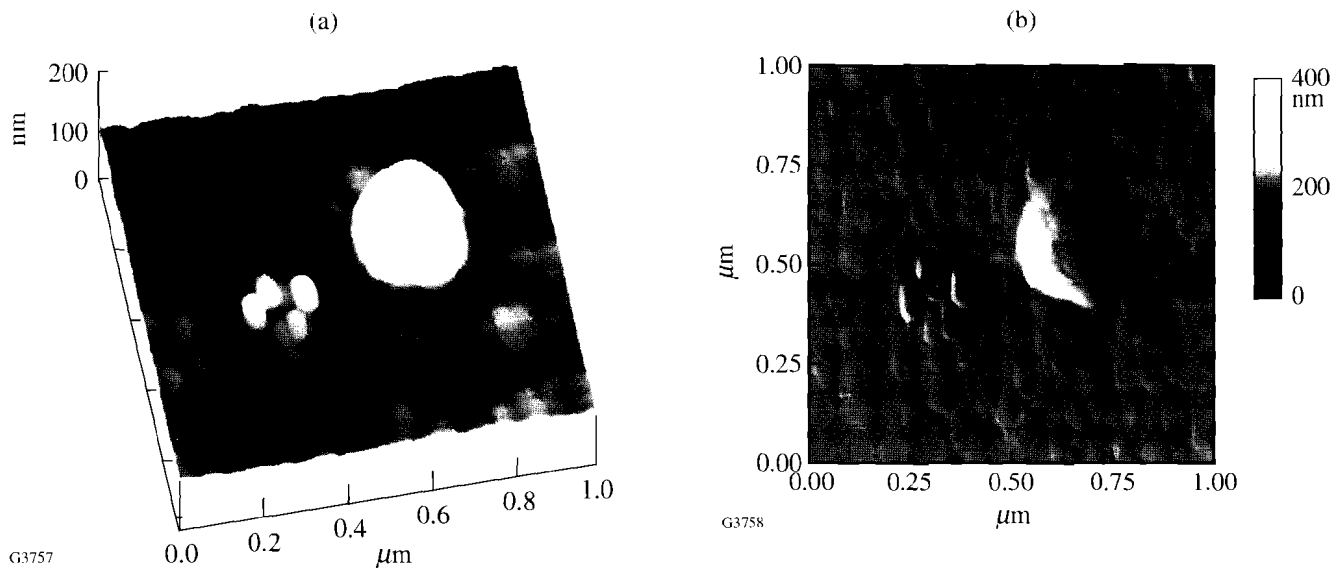


Figure 62.5  
(a) Crater formed in the vicinity of an unaffected nodular growth defect in the  $\text{HfO}_2/\text{SiO}_2$  film. The columnar structure of the nodule surface is masked by the saturating dome height ( $\sim 200$  nm) relative to the only 15-nm peak-to-valley excursions characteristic for the columnar structure. (b) High-pass filtered version of the image in Fig. 62.5(a), highlighting the columnar structure and nodular nature of the defect.

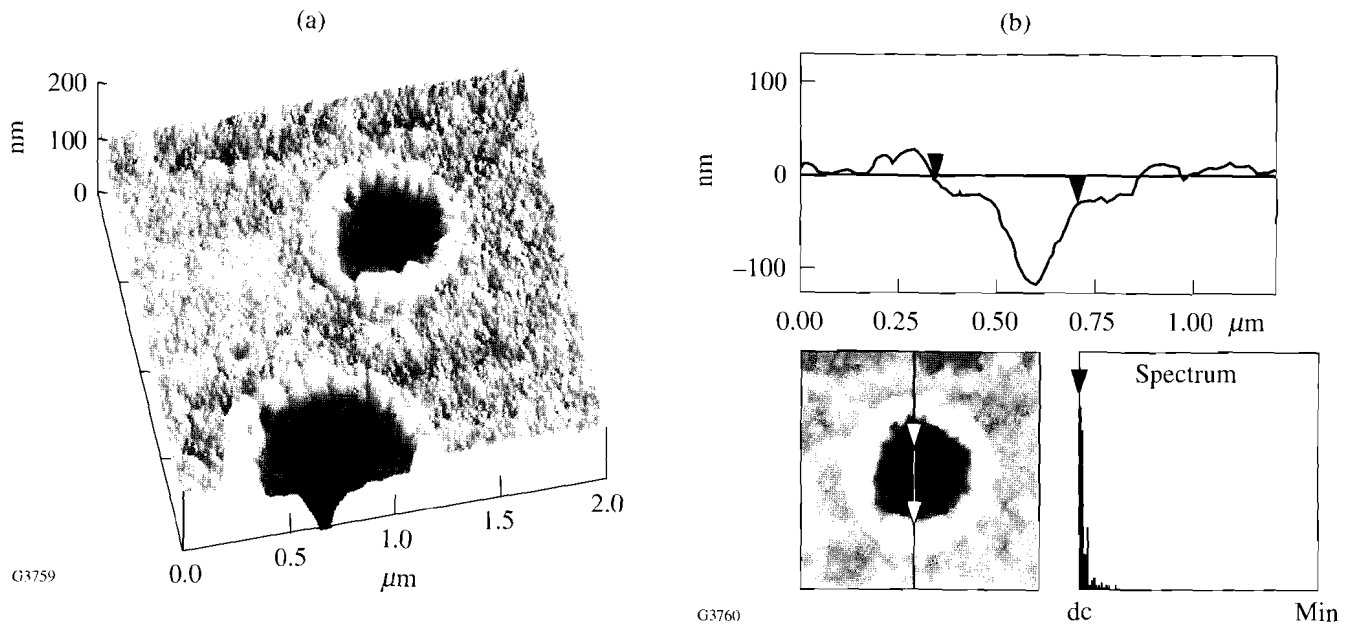


Figure 62.6

(a) Complex crater(s) in the  $\text{Sc}_2\text{O}_3/\text{SiO}_2$  film show the preserved columnar structure within the outer, larger-diameter cone. This indicates that melting remains localized within the inner cone volume, i.e., the  $\text{SiO}_2$  layer. (b) Cross section through the complex crater in the  $\text{Sc}_2\text{O}_3/\text{SiO}_2$  film. The double-cone structure is clearly pronounced here, as well as the 32.8-nm step formed by the outer cone.

structure with ridges elevated above the film surface average (Fig. 62.7). In complex craters, the inner, deeper cone also shows smooth, glassy walls, while the outer cone and the horizontal interface clearly preserve columnar structure. Although the horizontal step between the outer and inner cones occurs reproducibly at  $32.8 \pm 0.3$  nm from the nominal top surface average (36 craters were sampled for this value by AFM determination) and intuitively corresponds to the  $\text{Sc}_2\text{O}_3/\text{SiO}_2$  interface, the top-layer ( $\text{Sc}_2\text{O}_3$ ) physical thickness determined during evaporation by quartz-microbalance and optical-monitoring methods is supposed to be  $25.4 \pm 3$  nm. We ascribe this discrepancy to the uncertainty in material-density and refractive-index values for evaporated thin films when extracting physical thickness data from mass deposition and interference numbers.

Without detailed simulation, it remains unclear whether the observed double-cone damage is driven by starting events in the first or the second layer. In each scenario, the large difference in melting temperature between  $\text{SiO}_2$  ( $T_m = 1753^\circ\text{C}$ ) and  $\text{Sc}_2\text{O}_3$  ( $T_m \sim 2400^\circ\text{C}$ ) is essential in explaining the observed morphology. As the  $\text{SiO}_2$  crater walls yield no columnar-structure indicators, we can assume that melting has occurred in the  $\text{SiO}_2$  layer. Conversely, the columnar spatial frequencies typical of the unirradiated film are maintained around the

$\text{Sc}_2\text{O}_3$  crater walls and ridges, which rules out large-scale melting in that layer [Fig. 62.6(a)]. Temperatures insufficient for melting in  $\text{Sc}_2\text{O}_3$  are adequate to produce thermal expansion and possible buckling of the 25- to 32-nm top layer that, with or without further pressure from the underlying, melted  $\text{SiO}_2$  layer, severed along grain boundaries and “popped out.” In the event that the initiating absorber was lodged in the second ( $\text{SiO}_2$ ) layer, the melting of that layer preceded the thermal distortion of the top layer. If the absorber was instead in the top layer, heat from that layer must first propagate across the layer boundary at a flow rate that supports melting of  $\text{SiO}_2$  columns before the top layer pops out. On the basis of post-mortem evidence alone, the dominant or most likely mechanism cannot be determined with any certainty.

Superimposed, double-crater damage is absent in the  $\text{HfO}_2/\text{SiO}_2$  system. Conventional craters become more numerous and, if sufficiently adjacent to one another, merge as the level of damage increases in this system (Fig. 62.8). In spite of earlier reports to the contrary<sup>8</sup> that rank quarter-wave layers of  $\text{SiO}_2$  at nearly a factor of 2 higher in 351-nm thresholds than equivalent  $\text{HfO}_2$  layers of the same thickness, all merging craters in our samples originate in the  $\text{SiO}_2$  layer after exposure to fluences *above threshold*. This issue will be discussed in detail in the next section.

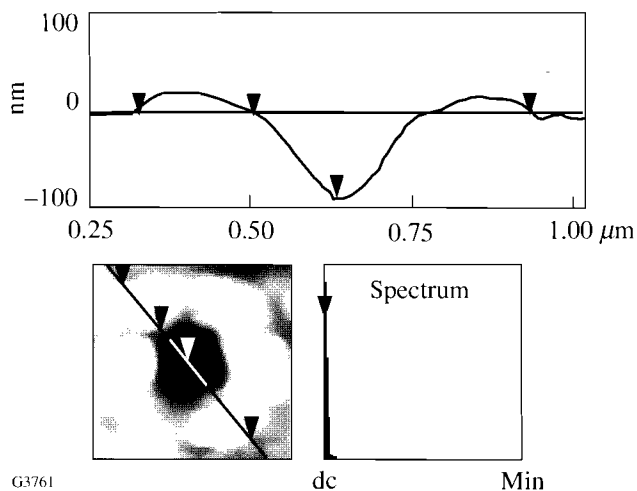


Figure 62.7  
Cross section through the 46-nm-deep conventional crater in the  $\text{Sc}_2\text{O}_3/\text{SiO}_2$  film. Smooth, glassy walls offer evidence of melting as part of the damage process.

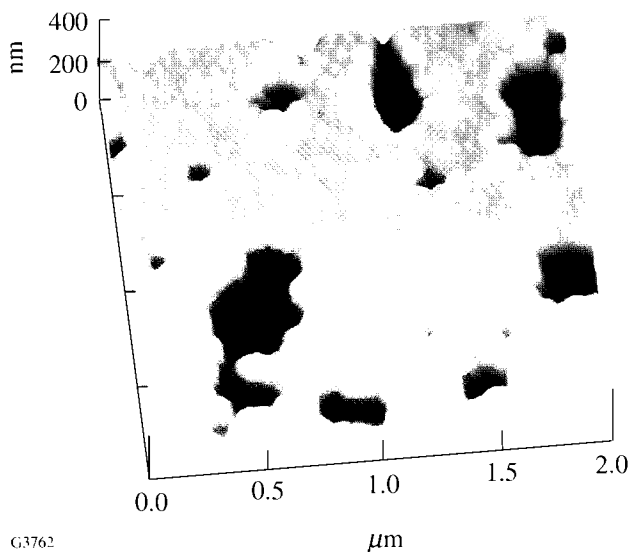


Figure 62.8  
Merging craters in the central portion of a moderate-damage event in the  $\text{HfO}_2/\text{SiO}_2$  film.

### 3. Crater-Depth Distribution

For both material systems, crater-depth distributions were recorded for three irradiation conditions: (1) weak damage, attained at fluences  $\sim 5\%$  above the threshold average; (2) moderate damage at  $15\%–20\%$  above threshold; and (3) the periphery condition of moderate damage, estimated to correspond to a fluence condition intermediate between (1) and (2). Damage-crater histograms were assembled using 10-nm-wide bins as a matter of convenience, with the under-

standing that for other bin sizes the crater-count distribution would vary. The arguments in the following sections are therefore not focused on exact depths, but rather on trends.

a.  $\text{HfO}_2/\text{SiO}_2$ . The weak-damage results summarized in Fig. 62.9 show that craters originate in the first or second layer only, with the majority originating in the 46-nm-thick  $\text{HfO}_2$  layer. The distribution peaks at a depth near 20 nm and shifts to greater depths with increasing fluence. At the periphery of moderate damage (Fig. 62.10), two peaks appear in the distribution at 30 nm and 80 nm, respectively; in the center of moderate damage, craters appear only infrequently in the  $\text{HfO}_2$  layer, while the distribution peak centers around 75 nm (Fig. 62.11). In the latter case, a few damage events originate near the interface between the second and third layers, but none were observed protruding into the next  $\text{HfO}_2$  layer. Concurrent with this shift of craters to greater depths is an increase in both their density (more than an order of magnitude higher for moderate damage than for near-threshold damage) and their tendency to merge.

Energy-balance considerations suggest that the amount of energy near threshold needed for removal of a cone volume (anticrater) is met predominantly by absorbers closer to the surface. We assume here that (1) the crater bottom is either at or very near the location of the absorbing defect, and (2) the defect characteristics and depth do not vary significantly from one AFM mapping area to the next. At energy values further above threshold, deeply located defects absorb sufficient energy to remove material and form a crater, while those closer to the surface not only cause material removal but also dissi-

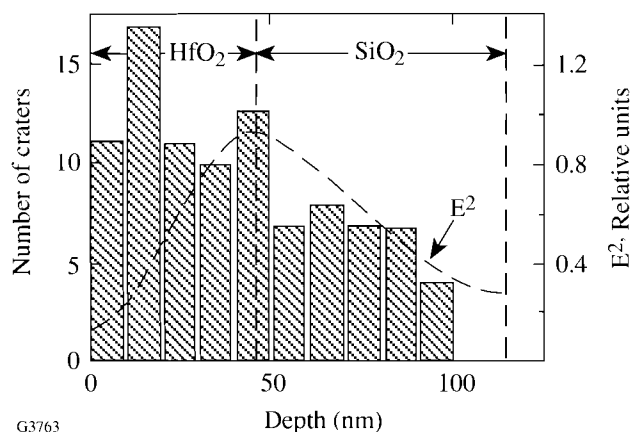


Figure 62.9  
Crater-depth distribution (histogram) for weak-damage conditions ( $\sim 5\%$  above threshold fluence) in the  $\text{HfO}_2/\text{SiO}_2$  system. The majority of craters originate within the top  $\text{HfO}_2$  layer.

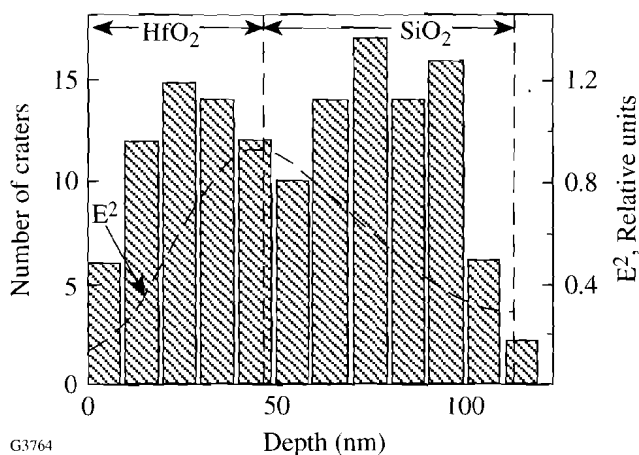


Figure 62.10 Crater-depth distribution (histogram) for moderate-damage (periphery) conditions in the HfO<sub>2</sub>/SiO<sub>2</sub> system. The second peak at 80-nm depth may be attributed to the combined effects of excess energy (relative to weak-damage conditions) and heat propagation from the higher-melting-point HfO<sub>2</sub> layer to the lower-melting-point SiO<sub>2</sub> layer.

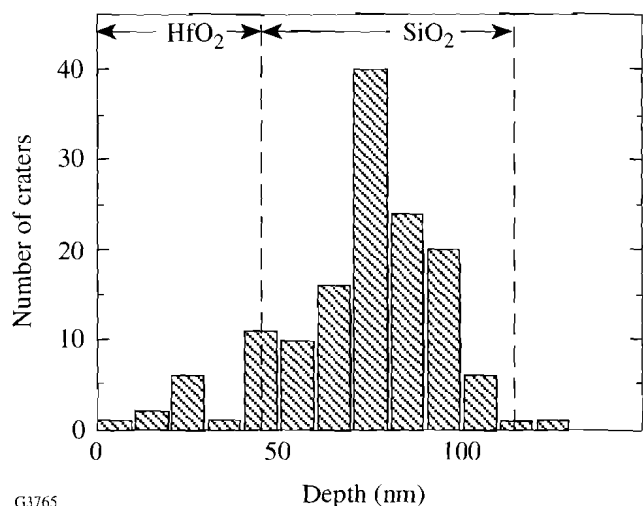


Figure 62.11 Crater-depth distribution at the central portion of a moderate-damage area (~20% above threshold fluence) in the HfO<sub>2</sub>/SiO<sub>2</sub> system. The distribution is now fully shifted into the SiO<sub>2</sub> layer, indicative of the dominance of heat-propagation effects under the 20%-above-threshold fluence conditions.

pate heat into the lower layer, extending the effective material modification to greater depths. This process is eased by the lower melting point of the second layer.

Figures 62.9 and 62.10 show also the E<sup>2</sup>-optical-intensity dependence inside the first two stack layers, which peak exactly at the interface. Other local maxima are located at the interface between the third and fourth layers, etc., with each

deeper maximum dropping in value relative to the previous one. In good coatings, it is therefore not surprising to find that, at values near threshold, only the absorbers near the largest intensity maximum contribute to crater formation.

It has long been suspected that, either for manufacturing reasons or owing to intrinsic physics, the discontinuities associated with interfacial areas are absorber locations themselves and, as such, are drivers for laser damage. The lack of any clear evidence for crater depths peaking at interfaces (the apparent interface peak in Fig. 62.9 is not nearly strong enough not to disappear after a small bin-size adjustment) suggest that, for state-of-the-art coatings, interface issues have ceased to be damage-critical issues.

b. Sc<sub>2</sub>O<sub>3</sub>/SiO<sub>2</sub>. In the Sc<sub>2</sub>O<sub>3</sub>/SiO<sub>2</sub> system the top Sc<sub>2</sub>O<sub>3</sub> layer is only 25.4 nm thick, and the peak of the E<sup>2</sup>-intensity distribution has been designed to not coincide with the layer interface. For this system, the intensity peaks at a depth of 65 nm. Both factors bias the crater-depth distribution toward the SiO<sub>2</sub> layer, as seen in Figs. 62.12 and 62.13 for the cases of weak damage and peripheral moderate damage. As was true for HfO<sub>2</sub>/SiO<sub>2</sub>, no craters originate from beneath the second layer. However, the shift of the distribution peak in going from weak to moderate damage (~40 nm in HfO<sub>2</sub>/SiO<sub>2</sub>) is more modest in this system. The 10-nm difference between distribution peaks in Figs. 62.12 and 62.13 is too small to be considered significant in light of the 10-nm bin width.

The trailing edges of the distributions shown in Figs. 62.12 and 62.13 drop faster with depth than the incident intensity,

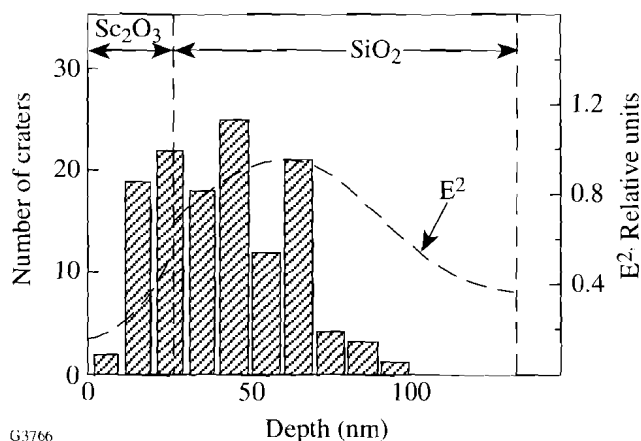
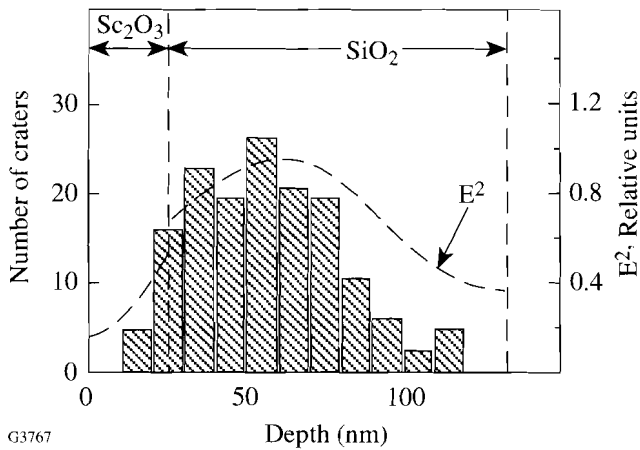


Figure 62.12 Crater-depth distribution (histogram) for weak damage in the Sc<sub>2</sub>O<sub>3</sub>/SiO<sub>2</sub> system. Owing to the relatively thin (25.4-nm) Sc<sub>2</sub>O<sub>3</sub> layer, the E-field, i.e., intensity, peaks inside the SiO<sub>2</sub> layer.



G3767

Figure 62.13

Crater-depth distribution (histogram) for moderate-damage (periphery) conditions in the  $\text{Sc}_2\text{O}_3/\text{SiO}_2$  system. The distribution is almost fully bracketed within the  $\text{SiO}_2$  layer.

which is not unexpected based on energy-balance grounds. If one simply assumes that for a conical crater to be formed the entire conical volume will be uniformly affected by heat, then the energy required for such heating will scale with the cone depth  $h$  as, at most,  $h^3$ . In reality, this dependence is probably less severe. The distribution's trailing edge already scales nearly as  $1/h^3$ , indicating that the exponent must be significantly smaller in light of the monotonously declining intensity dependence over the same depth interval.

### Conclusions

Mapping of pulsed-laser-induced damage morphologies in UV high-reflector coatings by AFM has shown the dominant damage feature to be submicron-lateral-sized craters that appear to be independent of micron-scale film growth defects (nodules). The local number density of these defect craters follows the intensity profile over the full laser-beam profile (hundreds of microns) but appears random over scale lengths of a few microns. The  $700^\circ\text{K}$  to  $1000^\circ\text{K}$  difference in the melting point between the high- and low-index medium in these stacks results in peculiar crater formation in the  $\text{Sc}_2\text{O}_3/\text{SiO}_2$  system, where crater-wall structural evidence shows melting and glass forming in the  $\text{SiO}_2$  layer, while the crater walls along the  $\text{Sc}_2\text{O}_3$  layer maintain columnar structure. A preponderance of craters originating in the second ( $\text{SiO}_2$ ) layer points toward heat transfer across the interface and lower-layer melting by absorbers located in the top layer as the primary cause. Together with the observation that the smallest measured craters allow for starting absorber sizes of  $<10$  nm, this distribution points toward randomly distributed nano-cluster

absorbers as the sources involved in the energy transfer from the optical field to the porous film medium. Whether these nano-clusters owe their absorptivity to unbound charges of metallic character or to charges localized in broken-stoichiometry states (point-defect states) remains to be resolved. The oxide deposition process certainly does not rule out bursts of impurity or non-stoichiometric events during which such nano-clusters could be dispersed into the coating stack. Similarly, at this time details of the damage kinetics are still speculative. The very low number density of nodules encountered leaves no doubt that few, if any, of these nano-clusters act as seeds for growth nodules, and that the nodules themselves may survive irradiation even though craters are formed within their immediate vicinity.

### ACKNOWLEDGMENT

This work was supported by the U.S. Department of Energy Office of Inertial Confinement Fusion under Cooperative Agreement No. DE-FC03-92SF19460, the University of Rochester, and the New York State Energy Research and Development Authority. The support of DOE does not constitute an endorsement by DOE of the views expressed in this article. This work was carried out on equipment of the Center for Optics Manufacturing (COM)—a DOD Center of Excellence by the U.S. Army Materiel Command.

### REFERENCES

1. M. R. Kozlowski *et al.*, in *Scanning Microscopy Instrumentation*, edited by G. S. Kino (SPIE, Bellingham, WA, 1991), Vol. 1556, pp. 68–78.
2. M. C. Staggs *et al.*, in *Laser-Induced Damage in Optical Materials: 1991*, edited by H. E. Bennett *et al.* (SPIE, Bellingham, WA, 1992), Vol. 1624, pp. 375–385.
3. M. C. Staggs *et al.*, in *Laser-Induced Damage in Optical Materials: 1992*, edited by H. E. Bennett *et al.* (SPIE, Bellingham, WA, 1993), Vol. 1848, pp. 234–242.
4. R. J. Tench, R. Chow, and M. R. Kozlowski, in *Laser-Induced Damage in Optical Materials: 1993*, edited by H. E. Bennett *et al.* (SPIE, Bellingham, WA, 1994), Vol. 2114, pp. 415–425.
5. K. L. Westra and D. J. Thomson, *J. Vac. Sci. Technol. B* **12**, 3176 (1994).
6. S. Papernov and A. Schmid, "A Comparison of Laser-Induced Damage Morphology in Three Model Thin-Film Systems:  $\text{HfO}_2$ ,  $\text{Y}_2\text{O}_3$ , and  $\text{Ta}_2\text{O}_5$ ," to be published in SPIE's *Laser-Induced Damage in Optical Materials: 1994*.
7. W. H. Lowdermilk and D. Milam, *IEEE J. Quantum Electron.* **QE-17**, 1888 (1981).
8. T. W. Walker, A. H. Guenther, and P. E. Nielsen, *IEEE J. Quantum Electron.* **QE-17**, 2041 (1981).